Ar implantation beneath graphene on Ru(0001): Nanotents and "can-opener" effect

Cun, Huanyao ; Iannuzzi, Marcella ; Hemmi, Adrian ; Osterwalder, Jürg ; Greber, Thomas

Abstract: Exposing a monolayer of graphene on ruthenium (g/Ru(0001)) to low energy Ar+ ions leads to nanotent formation and "can-opener" effect, similar phenomena as observed for h-BN/Rh(111) targets (Cun, Iannuzzi, Hemmi, Roth, Osterwalder and Greber, 2013). Nanotents are extra protrusions in the sp2 monolayers beneath which atoms are immobilized at room temperature. Annealing the Ar+ implanted structures results in the "can-opener" effect, i.e., the formation of voids with a diameter of about 2 nm within the graphene layer. The voids preferentially settle in the "hill" regions of the g/Ru(0001) superstructure and thus display spacial selectivity. This provides a convenient method to control defect positions within graphene membranes with nanometer precision. The results are obtained by scanning tunneling microscopy, low energy electron diffraction and photoemission, and are backed with density functional theory calculations.

DOI: https://doi.org/10.1016/j.susc.2014.11.004

Originally published at:
Cun, Huanyao; Iannuzzi, Marcella; Hemmi, Adrian; Osterwalder, Jürg; Greber, Thomas (2015). Ar implantation beneath graphene on Ru(0001): Nanotents and "can-opener" effect. Surface Science, 634:95-102.
DOI: https://doi.org/10.1016/j.susc.2014.11.004

Ar implantation beneath graphene on Ru(0001): nanotents and "can-opener" effect

Huanyao Cun[a], Marcella Iannuzzi[b], Adrian Hemmi[a], Jürg Osterwalder[a], Thomas Greber[a,*]

[a] *Physik-Institut, Universität Zürich, Winterthurerstrasse 190, CH-8057 Zürich, Switzerland*
[b] *Institute of Chemistry, Universität Zürich, Winterthurerstrasse 190, CH-8057 Zürich, Switzerland*

Abstract

Exposing a monolayer of graphene on ruthenium (g/Ru(0001)) to low energy Ar^+ ions leads to: nanotent formation and "can-opener" effect, similar phenomena as observed for h-BN/Rh(111) targets [1]. Nanotents are extra protrusions in the sp^2 monolayers beneath which atoms are immobilized at room temperature. Annealing the Ar^+ implanted structures results in the "can-opener" effect, *i.e.*, the formation of the voids with a diameter about 2 nm within the graphene layer. The voids preferentially settle in the "hill" regions of the g/Ru(0001) superstructure and thus display spacial selectivity. This provides a convenient method to spatially control defect positions within graphene membranes with nanometer precision. The results are obtained by scanning tunneling microscopy, low energy electron diffraction and photoemission, and are backed with density functional theory calculations.

Keywords: graphene, implantation, defect, "can-opener" effect, scanning tunneling microscopy

*Corresponding author
Email address: greber@physik.uzh.ch (Thomas Greber)
URL: +41 44 6355704 (Thomas Greber)

Introduction

Graphene [2] and hexagonal boron nitride (h-BN) [3] are novel two-dimensional (2D) layered materials, which are atomically thin. They have unique properties, such as remarkable mechanical strength, high optical transparency, good thermal conductivity and excellent chemical and thermal stability. In view of electronic properties, graphene sparkles with a high carrier mobility and it is a zero band gap semiconductor [4], while h-BN is a wide band gap insulator with optoelectronic promises [5]. Thus graphene and h-BN have a large potential for applications in electronic devices. However, many proposed applications of graphene require the ability to tune its electronic structure at the nanoscale [4]. Even though charge transfer [6, 7], doping and intercalation [8, 9, 10] can be applied to manipulate charge carrier concentrations and functionality, implementation with nanometer precision and high throughput remains a challenge.

Pristine, defect-free graphene is impermeable to gases including helium [11], theoretical models predict that graphene membranes with controlled-size and density of defects would exhibit selectivity and permeability orders of magnitude better than current filtration membranes [12, 13, 14]. Thus, spatial control of defect creation, self-assembly and annihilation in graphene at the nanoscale [15] is extremely important for the full exploration of this 2D material. Yet, experimental studies illustrating such ionic (molecular) selectivity and permeability have so far been limited to microscopic samples due to many challenges [16, 17], such as the quality of the graphene. Currently, among different methods to prepare atomically thin graphene and h-BN, chemical vapor deposition (CVD) has been demonstrated to be the most promising to prepare good quality graphene and h-BN. Interestingly, such sp^2 monolayers formed by CVD on a variety of substrates [18, 19, 20, 21, 22, 23, 24, 7, 25] exhibit superstructures with a few nanometers lattice constants. Beyond chemical approaches [26], it was realized that also defects created by ion irradiation induce new functionalities [27, 28], or ways to form new nanostructures [1, 29, 30, 31].

Besides graphene on iridium [19, 32, 29], graphene on ruthenium (0001)

(g/Ru(0001)) is among the best studied systems with a high Z metal substrate [20, 33, 21, 34]. The superstructure is by now commonly called "moiré" pattern. The supercell is divided into three different regions with different registries of the carbon atoms to the Ru atoms in the first substrate layer [23]. Two of these regions, where one of the two carbon atoms of the 1×1 honeycomb unit cell of graphene bind to a Ru atom are called "valley" and the third region is named as "hill", where the carbon does not bind to the substrate, but is stabilized by the strong sp^2 σ-bonds. The hill-hill distance is about 3 nm and related to the lattice mismatch of the graphene and ruthenium. Intriguingly, x-ray diffraction indicated a (23×23) super-cell with 4 hills [35], which could be observed with scanning tunneling microscopy (STM) and calculated with density functional theory [36].

In previous work, we reported the formation of Ar and Rb nanotents by exposing low energy ions to the h-BN/Rh(111) nanomesh [1, 37]. The immobilization of atoms occurs at two distinct sites beneath the "wire crossings" of the h-BN nanomesh honeycomb [38]. Annealing the ion-implanted nanostructure leads to the "can-opener" effect [1]: That is, the formation of highly regular voids with 2 nm diameter within a h-BN monolayer upon an annealing process. The density of these 2 nm voids can be modified by the Ar^+ ion dose prior to annealing. Furthermore, we explored the annihilation of the voids by annealing the h-BN/Rh(111) above 1000 K [31]. Here, combining STM, low energy electron diffraction (LEED) and photoemission, we demonstrate that by the exposure of low energy Ar^+ ions to CVD g/Ru(0001), Ar nanotents are formed in a similar way as on h-BN/Rh(111), and that they are also site-selective. Upon annealing of the implanted structure, the "can-opener" effect occurs on g/Ru(0001) as well, *i.e.*, we observe the formation of regular 2 nm voids in the graphene. These results pave a new route for the fuctionlization of graphene, and will eventually allow engineering of porous graphene membranes for practical applications, such as DNA sequencing [39], nanofiltration [26], water purification and desalination [40].

Results and Discussion

Our starting point was the preparation of a perfectly clean graphene monolayer on Ru(0001). The Ru(0001) crystal is cleaned by several cycles of Ne^+ ion sputtering at 1.5 keV in ultra high vacuum, followed by subsequent annealing to 1100 K, O_2 dosing and further flash to 1300 K. The cleanness of the Ru(0001) surface was checked by STM, LEED and x-ray photoelectron spectroscopy (XPS). Afterwards, the pristine graphene monolayer was grown on the clean Ru(0001) surface by high-temperature CVD of ethylene (C_2H_4) precursor molecules [23].

Figure 1a shows the large-area STM image of graphene on Ru(0001) at room temperature. Due to the lattice mismatch between graphene and Ru(0001) (the lattice constants of graphene and Ru are 0.249 nm and 0.272 nm, respectively), g/Ru(0001) forms a corrugated moiré pattern [20, 34, 36], as illustrated in Figure 1b. The average periodicity of the moiré pattern is about 3 nm for a unit cell with one hill, *i.e.*, about one quarter of the unit cell in Ref. [35, 36]. Roughly, a super-cell with a single moiron contains 12 $\times$ 12 carbon pairs above 11 $\times$ 11 Ru atoms, as the black frame shows in the inset of Figure 1a. The base of freestanding graphene has two identical carbon atoms C_A and C_B, which become distinguishable by the local coordination to the Ru substrate. The super-cell consists of three different regions [23]: the bright or weakly bound region (hill site, (C_A,C_B)=(hcp,fcc), also called atop site), a dark or strongly bound region (valley A, (C_A,C_B)=(fcc,top), short for hcp site, marked with blue triangle in Figure 1a), and an intermediate region (valley B, (C_A,C_B)=(top,hcp), short for fcc site, marked with a green triangle in Figure 1a). Figure 1c displays the cross-section along the white line in Figure 1b, which goes through the hcp site, hill site and fcc site three times sequentially. The apparent STM hill height varies, depending on tip conditions and tunneling parameters [20, 41], from 0.06 nm to 0.15 nm, where Figure 1c shows an average STM hill height of about 0.14 nm.

The sharp hexagonal (1 $\times$ 1) LEED patterns at 75 eV in Figure 2a demonstrate the highly ordered clean Ru(0001) surface. After CVD growth, the

g/Ru(0001) surface displays additional diffraction satellite-spots around the six principle spots of Ru. These additional sharp spots show the same hexagonal arrangement (Figure 2b), indicating that a highly ordered graphene monolayer has been formed on the Ru surface. In order to further check the graphene quality, Al Kα ($\hbar\omega$=1486.6 eV) XPS measurements have been carried out. Figure 2c displays the Ru $3d_{5/2}$ and Ru $3d_{3/2}$ core levels of the clean Ru(0001) (pink), g/Ru(0001) (green) and their differences (black, enhanced by a factor of four for clarity). Obviously, the graphene formation on Ru(0001) decreases the intensities of the Ru 3d peaks while a positive peak displays in the difference spectrum at around 286 eV and indicates the C 1s core level of graphene.

When the pristine graphene (Figure 3a) is exposed to low energy Ar^+ ions (sputter charge density of 460 nC/cm^2), the ions penetrate the graphene monolayer by consuming energy and accumulate above the Ru(0001) surface to form the so-called "nanotent" structures [1, 38, 31], as shown in Figure 3b. At room temperature the nanotents appear as bright protrusions in the STM topography image. These nanotents are a robust feature and may be observed at positive and negative tunneling voltages. They are stable at room temperature and also survive exposure to air. Interestingly, the ion implantation is a site-selective process. For h-BN/Rh(111), nanotents only form beneath two distinct nanomesh wire-crossing-sites, but not in the pores [1]. However, for g/Ru(0001), the situation varies due to the different structure and carbon bonding to the substrate of graphene, as compared to BN. Figure 3a and 3b show STM data of the graphene before and after exposure to low energy Ar^+ ions. The zoom-in room-temperature STM image in Figure 3c illustrates the graphene surface with a nanotent density of 0.7 protrusions per 11×11 Ru unit cell. They stop not only at hill sites, but also at fcc and hcp sites. Yet, the statistics of nanotent positions for Figure 3c indicates about half of the nanotents to locate beneath hill sites, 30 % at fcc sites and about 20 % at hcp sites. This is consistent with the density functional theory (DFT) calculations, which reveal the implantation energy for a nanotent at the hill site of at least (3.13 eV), at the fcc site it is intermediate(3.90 eV) and at the hcp is the maximum (4.30 eV). Details refer

to the theory part and table 1.

Figure 3d and 3e show the corresponding current and topography STM images with atomic resolution. Ar atoms not only immobilize beneath the hill site of the graphene moiré pattern, but also at the intermediate fcc site, as marked with light blue circles in Figure 3e. The ion bombardment knocks out carbon atoms, leaving vacancy defects within the graphene layer, which are marked with pink dashed circles in Figure 3e. Comparison of Figure 3a and 3b indicates that the height of most hills remains the same. However, there are some brighter protrusions on the implanted graphene surface. These brighter (higher) protrusions are attributed to the nanotents that settle at the hill sites. One example is the brightest protrusion in Figure 3e, by which both white cut-lines pass. In addition, the nanotents at valley sites also raise the height of the valley, which induces strain and makes the moiré pattern not perfectly regular, as displayed in Figure 3e (agrees with the LEED pattern in Figure 4b). The nanotents in the valleys appear smaller than those at the hill sites. Figure 3f and 3g display the two line profiles in Figure 3e that shows the height as measured from the bottom of the hcp site. The line in Figure 3f crosses an occupied fcc site, an empty hcp site, an occupied hill (atop) site and and an empty atop site, while the cut shown in Figure 3g passes by sequentially one vacancy defect (pink arrow), empty atop site, another vacancy defect (pink arrow) and occupied atop site. The average height of the nanotents is about 0.15 nm.

In order to check changes on the macroscopic scale, before and after Ar^+ ion exposure, a series of LEED measurements have been carried out for the same sample. Figure 4a-4f show the LEED patterns for pristine graphene (Figure 4a, 4b), Ar implanted graphene (Figure 4c, 4d) and implanted graphene after annealing to 1000 K (Figure 4e, 4f). Among these LEED patterns, Figure 4a, 4c and 4e are measured with an electron energy of 15 eV, while Figure 4b, 4d and 4f are taken at 74 eV. Clearly, the Ar^+ ion implantation process alters graphene surface structure as seen by LEED, as indicated in Figure 4c and 4d. After Ar implantation, the sharp hexagonal spots of graphene monolayer become weak and almost invisible at low energy (15 eV). This indicates that the

ordered graphene surface is altered due to the nanotent formation, which agrees with STM results. However, the LEED patterns at 74 eV are less affected and illustrate that the 1×1 order of graphene persists. If the implanted graphene surface is annealed to 1000 K, the highly ordered graphene surface recovered, and LEED measurements both at 15 eV and 74 eV show sharp diffraction spots of ordered graphene surface again (Figure 4e and 4f).

The chemical identification of the implanted species was performed with Al Kα ($\hbar\omega$=1486.6 eV) XPS, as displayed in Figure 4g. In order to exclude the influence of the sputter-cleaning process, the Ru(0001) crystal is sputter-cleaned by several cycles of Ne^+ ions. In Figure 4g, the green line shows no Ar signal on pristine graphene surface. The blue curve nicely displays the Ar 2p peaks, indicating the formation of Ar nanotents between the graphene monolayer and Ru(0001) substrate. When the Ar implanted graphene sample is annealed to 1000 K, Ar nanotents disappear from the surface, and some regular 2 nm voids appear within graphene layer due to so-called "can-opener" effect, which will be described later. Intriguingly, XPS indicates no significant intensity decrease of the Ar 2p peaks, as shown in the red curve in Figure 4g, and the core level of Ar $2p_{3/2}$ (241.9 eV) shifts towards lower binding energy by 50 meV upon annealing, which is at variance to the *h*-BN situation. For annealed *h*-BN/Ar/Rh(111), the core level binding energy of Ar $2p_{3/2}$ increases 300 meV to higher binding energy [1]. The difference between *h*-BN and graphene might owe to the structure difference and the different interactions between *h*-BN with Rh(111), and graphene with Ru(0001).

From the XPS atomic ratio of argon and carbon, we determine a coverage of 3 Ar atoms per 11×11 super cell. A similar ion dose shows a nanotent of 0.4 protrusions per super-cell. This indicates that for this relatively large Ar dose, the protrusions may host more than one Ar atom. The above findings are in line with angular resolved photoelectron spectroscopy (ARUPS) as well (Figure 4h), where the σ band at 5.9 eV and the π band at 10.0 eV of graphene are influenced by the Ar^+ exposure. The intensity decreases and the graphene related peaks broaden. Interestingly, the σ band shifts to higher binding energy

(from 5.9 eV to 6.6 eV) while the π band shifts in the opposite direction, *i.e.*, to lower binding energy (from 10.0 eV to 9.7 eV). Surprisingly, the intensity and width of these two bands recover after annealing an implanted graphene surface to 1000 K. The positions of the peaks get restored as well, which indicates the disappearance of the nanotents from the surface.

To better understand the Ar^+ ion implantation, DFT calculations based on the Gaussian and plane wave (GPW) formalism [42, 43] were performed. We used a slab model consisting of six Ru(0001) layers terminated by one carbon monolayer. The lateral dimensions correspond to 11×11 units of the hexagonal 2D lattice of Ru(0001), with lattice constant of 0.2718 nm. A 12 × 12 graphene layer is positioned on one side of the slab, in order to reproduce the unit cell of the moiré pattern. Periodic boundary conditions are always applied. The optimization of the structure leads to the corrugation of the initially flat and stretched (a = 0.249 nm) graphene layer. In agreement with experiment, we observe the formation of the triangular shaped hill, where (C_A,C_B)=(hcp,fcc), surrounded by the lower valley region, where one C atom per pair is atop. Figure 5c shows the top view of the periodically replicated g/Ru moiré structure together with the Tersoff-Hammann (TH)[44] simulation of the STM image, as calculated for a bias potential of -1eV. As the color map indicates, the hill maximum (green) is about 0.14 nm higher than the bottom of the valley region (hcp, blue). The profile of the TH iso-current surface taken along the displayed dashed line is reported in Figure 5b (top panel). It reproduces the height modulation running over the different registries, hcp, fcc, and atop, *i.e.*, going from the valley region, where the C atoms strongly interact with the substrate, to the hill.

Starting from the optimized g/Ru structure, Ar has been added at three different initial sites between graphene and Ru(0001), to simulate the implanted g/Ar/Ru(0001) system. The Ar atom can be easily stabilized beneath the hill region. The resulting graphene pattern is almost unchanged with respect to the bare g/Ru, but for the increased height of about 0.1 nm of the hill maximum. A 3D overview of the replicated unit cell of the implanted moiré structure, with

Ar at the hill site, is shown in Figure 5a. The corresponding top view and simulated STM are in Figure 5d, while the profile of the iso-current surface along the diagonal is reported in the middle panel of Figure 5b. The Ar atom occupies a fcc site, *i.e.*, directly under the central C atom of the hill. The total energy difference (implantation energy) with respct to the bare moiré structure plus one Ar atom in vacuum, is $\Delta E = +3.13$ eV per unit cell. Hence, Ar is trapped in a metastable state, corresponding to a local minimum of the additional strain in the graphene layer and the substrate. The energy loss due to the g/Ru modification, $\Delta E_{g/Ru}$, amounts to 1.36 eV, of which 1.25 eV is the energy cost for the additional strain in the graphene layer, ΔE_g. By inserting the Ar atom at the fcc region, it moves to a fcc site, *i.e.*, just below the center of a C-ring in the center of the fcc area. The presence of Ar generates a up-lifting of part of the layer, which results in a second and higher protrusion in the simulated STM image, as shown in Fiugure 5b (bottom) and 5e. The larger implantation energy $\Delta E = +3.90$ eV can be explained due to substantial deformation of the g/Ru system, $\Delta E_{g/Ru} = 1.90$ eV. We notice that, at this site, the implantation also reduces the attractive interaction between the substrate and graphene. Finally, according to the DFT model, the implantation beneath the hcp region further destabilizes the system, because affects even more strongly the binding of graphene to the substrate. It has to be taken into account that the limited size of our model implies the presence of one implanted Ar atom per unit cell. The Ar atom moves away from the hcp area towards the fcc region, until it stops at one fcc site similar to the one described above (see Figure 5f). The larger ΔE of 4.30 eV is explained by the larger loss in attractive energy between graphene and Ru, since the graphene strain energy ΔE_g is approximately the same. These results are summarized in Table 1.

Remarkably, annealing of the implanted g/Ar/Ru(0001) system to 1000 K provokes a peculiar response: the Ar nanotents disappear from the graphene surface, highly regular voids with 2 nm diameter form in the monolayer, and some cut-out flakes appear on the surface. Figure 6 shows a g/Ru(0001) sample exposed to a sputter charge density of 350 nC/cm^2 after annealing to 1000 K.

Table 1: DFT results on the Ar implantation: minimum Ar-C distance d_{min} and peak-to-peak height difference computed from the TH iso-current surface are reported in nm. The implantation energy ΔE and its portion due to the structural change of the entire moiré, $\Delta_{g/Ru}$ or of the graphene layer only Δ_g, are reported in ev.

Sys.	d_{min}(Ar-C)	ΔE	$\Delta E_{g/Ru}$	ΔE_g	TH Δh
hill	0.254	3.13	1.36	1.25	0.24
fcc	0.273	3.90	1.90	2.63	0.22
hcp→fcc	0.273	4.30	2.20	2.59	0.22

No Ar nanotents can be observed, though 1.5 % of the hills map dark, and some large brighter flakes appear on the surface. We assign the flakes near the 2 nm voids to the cut-out from the hill sites during the annealing process, similar to a "lid" cut from a tin can, which lead us to call the formation process "can-opener" effect [1]. The cutting temperature is well below the one of g/Ru(0001) disintegration of 1700 K [20]. Figure 6b is the zoom-in image of the white square in Figure 6a, which displays the four cut-out hill sites on the surface. To explore the origin of the "can-opener" effect, the pristine g/Ru(0001) is annealed to the same temperature 1000 K. However, no such effect is observed. Therefore the "can-opener" effect must be related to the active species which are introduced by ion exposure.

It is noticed from Figure 3d and 3e that the ion bombardment leads not only to nanotent formation, but also generates vacancy defects, *i.e.*, knock out of carbon atoms from the graphene monolayer. At elevated temperature, these vacancy defects are expected to become active and even mobile. We discussed in a previous work the case of h-BN/Ar/Rh, where they diffuse and assemble at the rim of the nanomesh pores due to the minimum energy costs there, leading to a similar "can-opener" effect at 900 K [31]. For g/Ar/Ru, the required temperature to observe the "can-opener" effect is 1000 K, *i.e.*, higher than the temperature needed for the h-BN/Ar/Rh system. This indicates that the interactions between graphene and Ru(0001) substrate are stronger than

the ones between h-BN and Rh(111). This can be associated to the different σ-bond and element specific π-bond strength characterizing these two sp^2 monolayer/substrate systems. Additionally, this also suggests that the formation energy of defects within h-BN and graphene, as well as their preferential locations are different. The data in Figure 6 reveal that the cut-out takes place at the edges of the hill site, where the carbon atoms bridging between weakly bound-to-substrate and strongly bound-to-substrate area combine. In other words, the defects start to agglomerate at the edges of the hill site and finally become abundant enough there and lead to the "can-opener" effect. This results in the cut-out of the hill site, as displayed in the atomic resolution STM image in Figure 6c. It displays an annealed implanted graphene surface with a cut-out hill site, which maps darker. Scanning tunneling spectroscopy (STS) measurements (not shown here) indicate that the darker region with hexagonal lattice is Ru(0001) substrate. The image line profile in Figure 6d follows the white line in Figure 6c and illustrates the height difference of the normal hill site and the Ru substrate. The curved features of Ru atoms is owing to the finite sharpness of the tip.

Of course, the procedure of ion implantation and subsequent annealing can be repeated on the same g/Ru(0001) surface. This will lead to an accumulation of 2 nm voids within a graphene monolayer.

Conclusions

In conclusion, the controlled formation of nanotents and regular 2 nm voids at specific sites of graphene monolayer on a Ru(0001) substrate is reported. At room temperature, nanotents are stable beneath graphene monolayer. Annealing treatment of implanted graphene surface induces the "can-opener" effect, that is, cutting out of the hill flakes and form 2 nm voids within a single layer of graphene. Systematic measurements reveal that the nanotent formation and "can-opener" effect are well-controlled and repeatable processes. These results pave the way to practical applications of graphene, such as gasfiltration, desali-

nation and water purification.

Methods

Experimental

The experiments were performed in two ultrahigh-vacuum (UHV) systems with base pressure of 1×10^{-10} mbar. One is a variable-temperature scanning tunneling microscope (Omicron VT-STM), and the other has a room-temperature STM (Park Scientific) and low energy electron diffraction (LEED) combined with photoemission on the same sample[45, 46]. The STM measurements were carried out with electrochemically etched tungsten tips. All STM images were taken in constant-current mode at room temperature. The graphene samples were produced with the standard recipe [23], though the samples for the photoemission experiments were cleaned with Ne^+ ion sputtering. The ion implantation was achieved with a Specs IQP 10/35 Penning type ion sources run at lowest acceleration potential. The sputter charge density corresponds to the integrated sputter current density.

Theory

Calculations are performed using KohnSham DFT within the the GPW formalism as implemented in the Quickstep module in the CP2K program package [47, 48]. Dual-space pseudopotentials [49] are used to describe the interaction of valence electrons with atomic cores. The pseudopotential for carbon assume 4 valence electrons, and for Ru 8 valence electrons. The GPW scheme is based on the expansion of the molecular orbitals with contracted Gaussian basis functions, whereas the auxiliary plane wave basis set is applied for the solution of the Poisson equation in the reciprocal space. We use a cutoff of 500 Ry for the plane wave basis set and sample the Brillouin zone at Γ only. Exchange and correlation are calculated with the Perdew-Burke- Ernzerhof (PBE) GGA exchange-correlation functional. Corrections for the dispersion interactions are introduced following the DFT-D3 formalism [50].

Conflict of Interest

The authors declare no competing financial interest.

Acknowledgements

Financial support by the Swiss National Science Foundation, Forschungskredit funding by University of Züric and support by the EC under the Graphene Flagship (contract no. CNECT-ICT-604391) is gratefully acknowledged. We thank the Swiss National Supercomputer Centre (CSCS) for the generous allocation of computer time and Gerson Mette for laboratory support.

References

[1] H. Y. Cun, M. Iannuzzi, A. Hemmi, S. Roth, J. Osterwalder, T. Greber, Immobilizing individual atoms beneath a corrugated single layer of boron nitride, Nano Lett. 13 (2013) 2098–2103.

[2] M. Batzill, The Surface Science of Graphene: Metal Interfaces, CVD Synthesis, Nanoribbons, Chemical Modifications, and Defects, Surf. Sci. Rep. 67 (3-4) (2012) 83–115. doi:{10.1016/j.surfrep.2011.12.001}.

[3] A. Pakdel, Y. Bando, D. Golberg, Nano boron nitride flatland, Chem. Soc. Rev. 43 (2014) 934–959.

[4] A. K. Geim, K. S. Novoselov, The rise of graphene, Nat. Mater. 6 (2007) 183–191.

[5] L. Song, L. Ci, H. Lu, P. B. Sorokin, C. Jin, J. Ni, A. G. Kvashnin, D. G. Kvashnin, J. Lou, B. I. Yakobson, P. M. Ajayan, Large scale growth and characterization of atomic hexagonal boron nitride layers, Nano Lett. 10 (2010) 3209–3215.

[6] T. Tseng, C. Urban, Y. Wang, R. Otero, S. L. Tait, M. Alcam, D. Écija, M. Trelka, J. M. Gallego, N. Lin, M. Konuma, U. Starke, A. Nefedov, A. Langner, C. Wöll, M. A. Herranz, M. Martín, N. Martín, K. Kern, R. Miranda, Charge-transfer-induced structural rearrangements at both sides of organic/metal interfaces, Nat. Chem. 2 (2010) 374–379.

[7] C. Coletti, C. Riedl, D. S. Lee, B. Krauss, L. Patthey, K. Klitzing, J. H. Smet, U. Starke1, Charge neutrality and band-gap tuning of epitaxial graphene on sic by molecular doping, Phys. Rev. B 81 (2010) 235401.

[8] A. B. Preobrajenski, M. L. Ng, N. A. Vinogradov, A. S. Vinogradov, E. Lundgren, A. Mikkelsen, N. Martensson, Impact of Oxygen Coadsorption on Intercalation of Cobalt under the h-BN Nanomesh, Nano Lett. 9 (7) (2009) 2780–2787. doi:{10.1021/nl901316p}.

[9] T. Brugger, H. Ma, M. Iannuzzi, S. Berner, A. Winkler, J. Hutter, J. Osterwalder, T. Greber, Nanotexture Switching of Single-Layer Hexagonal Boron Nitride on Rhodium by Intercalation of Hydrogen Atoms, Angew. Chem. Int. Ed. 49 (35) (2010) 6120–6124. doi:{10.1002/anie.201001064}.

[10] J. H. Mao, L. Huang, Y. Pan, M. Gao, J. F. He, H. T. Zhou, H. M. Guo, Y. Tian, Q. Zou, L. Z. Zhang, H. G. Zhang, Y. L. Wang, S. X. Du, X. J. Zhou, A. H. Castro Neto, G. H. J., Silicon layer intercalation of centimeter-scale, epitaxially grown monolayer graphene on ru(0001), Appl. Phys. Lett. 100 (2012) 093101.

[11] J. S. Bunch, S. S. Verbridge, J. S. Alden, A. M. van der Zande, J. M. Parpia, H. G. Craighead, P. L. McEuen, Impermeable atomic membranes from graphene sheets, Nano Lett. 8 (2008) 2458–2462.

[12] D. Jiang, V. R. Cooper, S. Dai, Porous graphene as the ultimate membrane for gas separation, Nano Lett. 9 (2009) 4019–4024.

[13] D. Cohen-Tanugi, J. C. Grossmanand, Water desalination across nanoporous graphene, Nano Lett. 12 (2012) 3602–3608.

[14] S. J. Zhao, J. M. Xue, W. Kang, Ion selection of charge-modified large nanopores in a graphene sheet, J. Chem. Phys. 139 (2013) 114702.

[15] A. W. Robertson, C. S. Allen, Y. A. Wu, K. He, J. Olivier, J. Neethling, A. I. Kirkland, J. H. Warner, Spatial control of defect creation in graphene at the nanoscale, Nat. Commun. doi: 10.1038/ncomms2141 (2012) 3:1144. doi:10.1038/ncomms2141.

[16] S. P. Koenig, L. Wang, J. Pellegrino, J. S. Bunch, Selective molecular sieving through porous graphene, Nat. Nanotechnol. 7 (2012) 728–732.

[17] S. P. Koenig, L. Wang, J. Pellegrino, J. S. Bunch, Molecule-hugging graphene nanopores, Proc. Nati. Acad. Sci. 110 (2013) 12192–12196.

[18] M. Corso, W. Auwärter, M. Muntwiler, A. Tamai, T. Greber, J. Osterwalder, Boron nitride nanomesh, Science 303 (2004) 217–220.

[19] A. T. N'Diaye, S. Bleikamp, P. J. Feibelman, T. Michely, Two-dimensional ir cluster lattice on a graphene moire on ir(111), Phys. Rev. Lett. 97 (21) (2006) 215501.

[20] S. Marchini, S. Günther, J. Wintterlin, Scanning tunneling microscopy of graphene on Ru(0001), Phys. Rev. B 76 (7) (2007) 075429. doi:{10.1103/PhysRevB.76.075429}.

[21] P. W. Sutter, J.-I. Flege, E. A. Sutter, Epitaxial Graphene on Ruthenium, Nat. Mater. 7 (5) (2008) 406–411.

[22] P. Sutter, S. J. T., E. Sutter, Graphene on pt(111): Growth and substrate interaction, Phys. Rev. B 80 (2009) 245411.

[23] T. Brugger, S. Günther, B. Wang, J. H. Dil, M.-L. Bocquet, J. Osterwalder, J. Wintterlin, T. Greber, Comparison of Electronic Structure and Template Function of Single-layer Graphene and a Hexagonal Boron Nitride Nanomesh on Ru(0001), Phys. Rev. B 79 (4) (2009) 045407. doi:{10.1103/PhysRevB.79.045407}.

[24] X. S. Li, W. W. Cai, J. An, S. Kim, J. Nah, D. X. Yang, R. Piner, A. Velamakanni, I. Jung, E. Tutuc, S. K. Banerjee, L. Colombo, R. S. Ruoff, Large-area synthesis of high-quality and uniform graphene films on copper foils, Science 324 (2009) 1312–1314.

[25] S. Joshi, D. Ecija, R. Koitz, M. Iannuzzi, A. P. Seitsonen, J. Hutter, R. Sachdev, S. Vijayaraghavan, F. Bischoff, K. Seufert, J. V. Barth, W. Auwärter, Boron nitride on cu(111): An electronically corrugated monolayer, Nano Lett. 12 (2012) 5821–5828.

[26] S. C. O'Hern, M. S. H. Boutilier, J.-C. Idrobo, Y. Song, J. Kong, T. Laoui, M. Atieh, R. Karnik, Selective ionic transport through tunable subnanome-

ter pores in single-layer graphene membranes, Nano Lett. 14 (2014) 1234–1241.

[27] M. M. Ugeda, I. Brihuega, F. Guinea, J. M. Gómez-Rodríguez, Missing atom as a source of carbon magnetism, Phys. Rev. Lett. 104 (2010) 096804.

[28] M. M. Ugeda, D. Fernández-Torre, I. Brihuega, P. Pou, A. J. Martínez-Galera, R. Pérez, J. M. Gómez-Rodríguez, Point defects on graphene on metals, Phys. Rev. Lett. 107 (2011) 116803.

[29] S. Standop, O. Lehtinen, C. Herbig, G. Lewes-Malandrakis, F. Craes, J. Kotakoski, T. Michely, A. Krasheninnikov, C. Busse, Ion impacts on graphene/ir(111): Interface channeling, vacancy funnels, and a nanomesh, Nano Lett. 13 (2013) 1948–1955.

[30] E. H. Å hlgren, S. K. Hämäläinen, O. Lehtinen, P. Liljeroth, J. Kotakoski, Structural manipulation of the graphene/metal interface with ar^+ irradiation, Phys. Rev. B 88 (2013) 155419.

[31] H. Y. Cun, M. Iannuzzi, A. Hemmi, J. Osterwalder, T. Greber, Two-nanometer voids in single-layer hexagonal boron nitride: Formation via the can-opener effect and annihilation by self-healing, ACS Nano 8 (2014) 7423–7431.

[32] C. Busse, P. Lazić, R. Djemour, J. Coraux, T. Gerber, N. Atodiresei, V. Caciuc, R. Brako, A. T. N'Diaye, S. Blügel, J. Zegenhagen, T. Michely, Graphene on ir(111): Physisorption with chemical modulation, Phys. Rev. Lett. 107 (2011) 036101.

[33] A. L. Vazquez de Parga, F. Calleja, B. Borca, M. C. G. Passeggi, Jr., J. J. Hinarejos, F. Guinea, R. Miranda, Periodically rippled graphene: Growth and spatially resolved electronic structure, Phys. Rev. Lett. 100 (5) (2008) 056807. doi:{10.1103/PhysRevLett.100.056807}.

[34] Y. Pan, H. G. Zhang, D. X. Shi, J. T. Sun, S. X. Du, F. Liu, H. J. Gao, Highly ordered, millimeter-scale, continuous,single-crystalline graphene monolayer formed on ru(0001), Adv. Mater. 21 (2009) 2777–2780.

[35] D. Martoccia, P. R. Willmott, T. Brugger, M. Björck, S. Günther, C. M. Schlepütz, A. Cervellino, S. A. Pauli, B. D. Patterson, S. Marchini, J. Wintterlin, W. Moritz, T. Greber, Graphene on ru(0001): A 25 × 25 supercell, Phys. Rev. Lett. 101 (2008) 126102.

[36] M. Iannuzzi, I. Kalichava, H. F. Ma, S. J. Leake, H. T. Zhou, G. Li, Y. Zhang, O. Bunk, H. J. Gao, J. Hutter, P. R. Willmott, , T. Greber, Moiré beatings in graphene on ru(0001), Phys. Rev. B 88 (2013) 125433. doi:10.1103/PhysRevB.88.125433.

[37] L. H. De Lima, H. Y. Cun, A. Hemmi, T. Kaelin, T. Greber, Note: An ion source for alkali metal implantation beneath graphene and hexagonal boron nitride monolayers on transition metals, Rev. Sci. Instrum. 84 (2013) 126104.

[38] H. Y. Cun, M. Iannuzzi, A. Hemmi, J. Osterwalder, T. Greber, Implantation length and thermal stability of interstitial ar atoms in boron nitride nanotents, ACS Nano 8 (2014) 1014–1021.

[39] Z. Zhou, Y. Hu, H. Wang, Z. Xu, W. L. Wang, X. D. Bai, X. Y. Shan, X. H. Lu, Dna translocation through hydrophilic nanopore in hexagonal boron nitride, Sci. Rep. 3 (2013) 3287.

[40] A. Siria, P. Poncharal, A. Biance, R. Fulcrand, X. Blase, S. T. Purcell, L. Bocquet, Giant osmotic energy conversion measured in a single transmembrane boron nitride nanotube, Nature 494 (2013) 455–458.

[41] B. Wang, M.-L. Bocquet, S. Marchini, S. Günther, J. Wintterlin, Chemical origin of a graphene moiré overlayer on ru(0001), Phys. Chem. Chem. Phys. 10 (2008) 3530–3534.

[42] G. Lippert, J. Hutter, M. Parrinello, A hybrid Gaussian and plane wave density functional scheme, Mol. Phys. 92 (3) (1997) 477–487.

[43] J. VandeVondele, M. Krack, F. Mohamed, M. Parrinello, T. Chassaing, J. Hutter, QUICKSTEP: Fast and Accurate Density Functional Calculations Using a Mixed Gaussian and Plane Waves Approach, Comput. Phys. Commun. 167 (2) (2005) 103–128. doi:{10.1016/j.cpc.2004.12.014}.

[44] J. Tersoff, D. Hamann, Theory of the Scanning Tunneling Microscope, Phys. Rev. B 31 (1985) 805–813. doi:10.1103/PhysRevB.31.805.

[45] T. Greber, O. Raetzo, T. Kreutz, P. Schwaller, W. Deichmann, E. Wetli, J. Osterwalder, A photoelectron spectrometer for k-space mapping above the Fermi level, Rev. Sci. Instrum. 68 (12) (1997) 4549–4554. doi:{10.1063/1.1148429}.

[46] W. Auwärter, M. Muntwiler, T. Greber, J. Osterwalder, Co on *h*-BN/Ni(111): from Island to Island-Chain Formation and Co Intercalation, Surf. Sci. 511 (1-3) (2002) 379–386. doi:{10.1016/S0039-6028(02)01545-5}.

[47] J. Hutter, M. Iannuzzi, F. Schiffmann, J. Vandevondele, cp2k: atomistic simulations of condensed matter systems, Wiley Interdisciplinary Reviews: Computational Molecular Science 4 (1) (2014) 15–25.

[48] CP2k Developers Group under the Terms of the GNU General Public Licence; see http://www.cp2k.org (2014).

[49] S. Goedecker, M. Teter, J. Hutter, Separable dual-space gaussian pseudopotentials, Phys. Rev. B 54 (3) (1996) 1703–1710.

[50] S. Grimme, J. Antony, S. Ehrlich, H. Krieg, A Consistent and Accurate Ab Initio Parametrization of Density Functional Dispersion Correction (DFT-D) for the 94 Elements H-Pu, J. Chem. Phys. 132 (15) (2010) 154104.

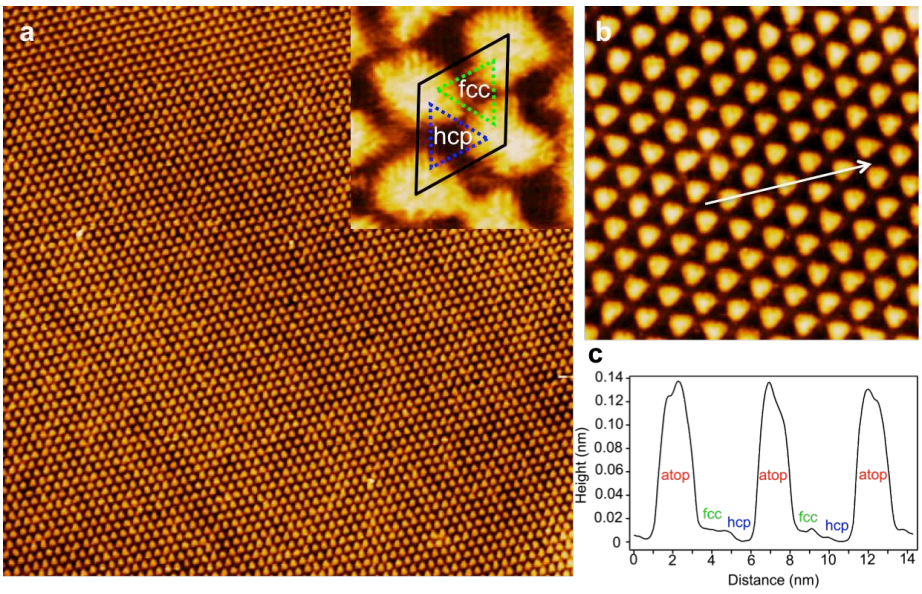

Figure 1: **Room-temperature STM images of g/Ru(0001).** (a) Large-area image (190×190 nm^2) of pristine g/Ru(0001), U_t = -1.20 V, I_t = 0.50 nA. The inset in (a) is atomic resolution STM image. The black frame represents the unit cell of graphene, containing one hill. It includes three regions: the most highest (bright) hill region (atop), the mediate region (green, fcc) and the lowest (dark) region (blue, hcp). (b) Zoom-in of (a) (28×28 nm^2) showing the hexagonal structure of graphene. The bright protrusions are hill sites. U_t = -1.20 V, I_t= 0.10 nA. (c) Cross-section along the white line in (b), which passes three atop regions (red), two fcc (green) and two hcp (blue) regions.

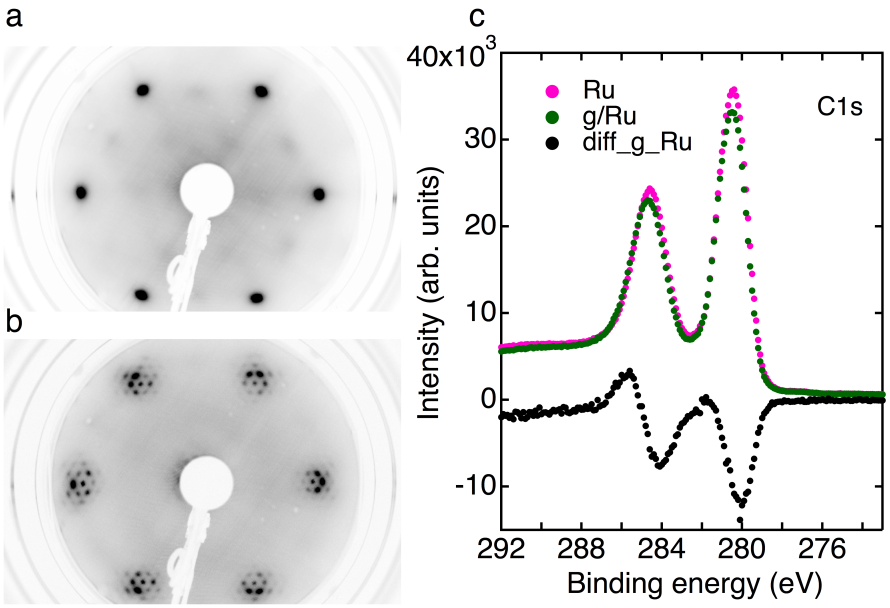

Figure 2: **LEED patterns and XPS of g/Ru(0001).** (a) LEED patterns of clean Ru(0001) surface. The electron energy is 75 eV. (b) LEED pattern of pristine g/Ru(0001) surface. The dark substrate spots are surrounded by the satellites spots, which shows hexagonal structure of the graphene monolayer. Electron energy is 80 eV. (c) Normal emission Al Kα ($\hbar\omega$=1486.6 eV) XPS of clean Ru(0001) (pink), g/Ru(0001) (green) and their differences (black), showing the core binding energy levels of the Ru $3d_{5/2}$ and Ru $3d_{3/2}$. Clearly, the graphene formation on Ru(0001) lows the two Ru 3d peaks. The difference which is multiplied by a factor of four for clarity, indicates an additional peak at around 286 eV, which corresponds to the C 1s core level of a graphene monolayer.

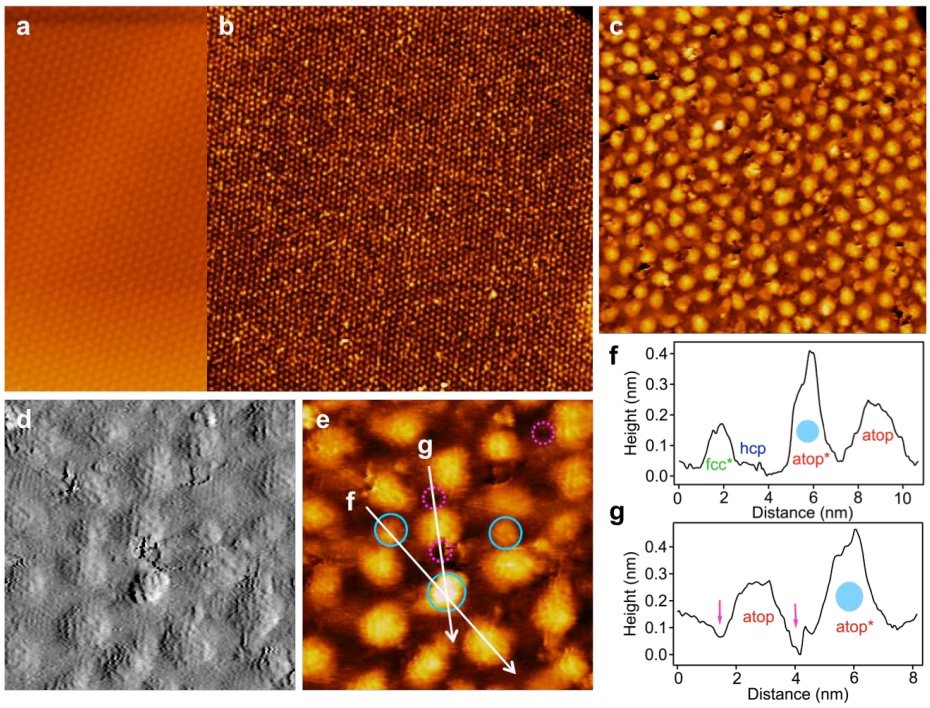

Figure 3: **Room-temperature STM data of ion-implanted Ar below g/Ru(0001).** (a) STM image (60×114 nm^2) of clean g/Ru(0001), U_t= -1.10 V, I_t = 0.50 nA. (b) Large-scale image (190×190 nm^2) with Ar induced protrusions, U_t = -1.20 V, I_t= 0.50 nA. (c) Zoom-in of (b) (47×47 nm^2) showing the Ar protrusions locate at different regions within graphene unit cell. U_t = -1.20 V, I_t= 0.20 nA. (d, e) Atomic-resolution STM current and topography images demonstrating Ar to be implanted beneath the graphene monolayer. The protrusions marked with blue circles are caused by interstitial Ar, and the pink circles indicate vacancy defects generated by the Ar penetration. 14×14 nm^2, U_t = -1.10 V, I_t= 0.20 nA. (f, g) Cross-section along the two white lines in (e). The line (f) passes an occupied fcc site, an empty hcp site, an occupied atop site and an empty atop site, while the line (g) indicates two vacancy defects (pink arrow), an occupied and an empty atop site.

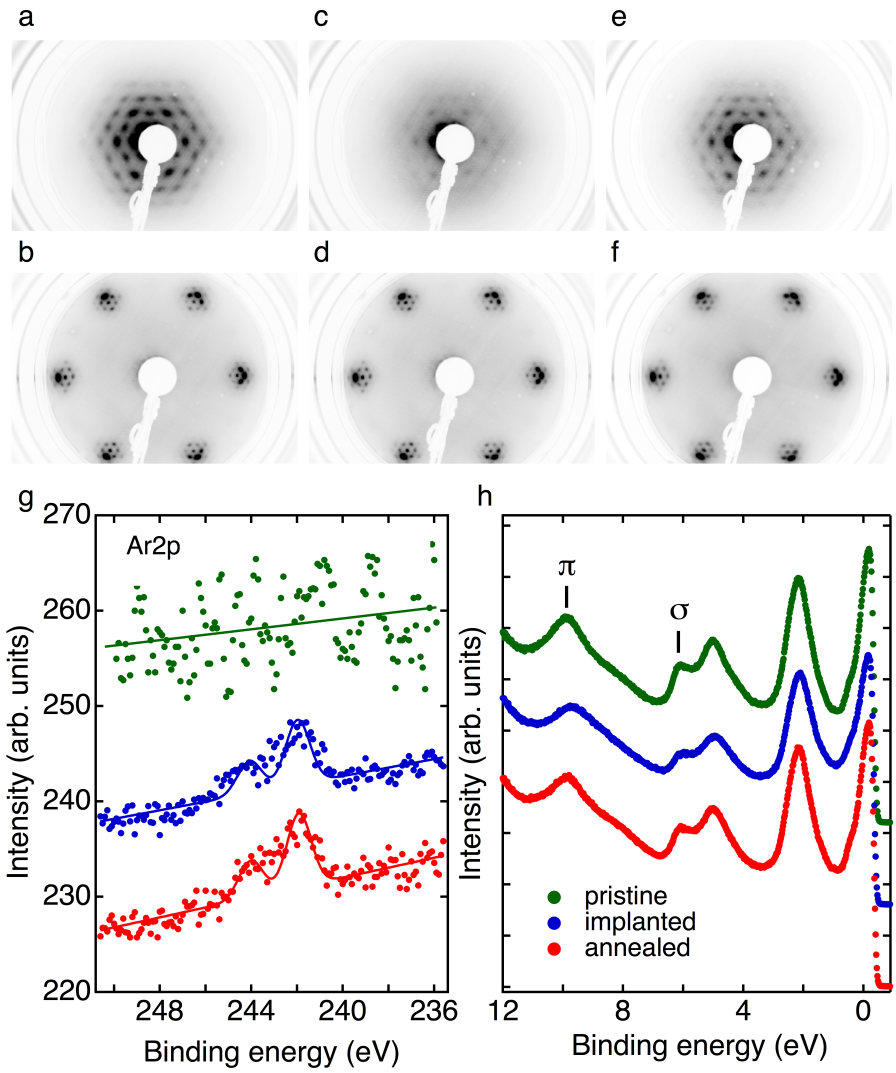

Figure 4: **LEED patterns and corresponding photoemission spectra of g/Ar/Ru(0001) before and after annealing to 1000 K.** (a-f) LEED patterns of pristine graphene (a, b), Ar implanted graphene (c, d) and aannealed implanted graphene to 1000 K (e, f). The electron energies are 15 eV (a, c, e) and 74 eV (b, d, f). The LEED pattern of implanted graphene at 15 eV demonstrates an obvious weakening of the hexagonal pattern compared to the pristine graphene. (g) Al Kα ($\hbar\omega$=1486.6 eV) XPS of Ar 2p core levels for pristine g/Ru(0001) (green), Ar implanted (blue) and after annealing (red). The Ar $2p_{3/2}$ binding energy of 241.9 eV shifts by 50 meV upon annealing, though the intensity is unaltered. (h) Normal emission UPS ($\hbar\omega$=21.2 eV) spectra of pristine g/Ru(0001) (green), Ar implanted (blue), and after annealing (red). The blue spectrum features a distinct broadening and intensity decrease of the σ and π bands. The peaks recover after annealing to 1000 K. The curves are vertically offset for clarity.

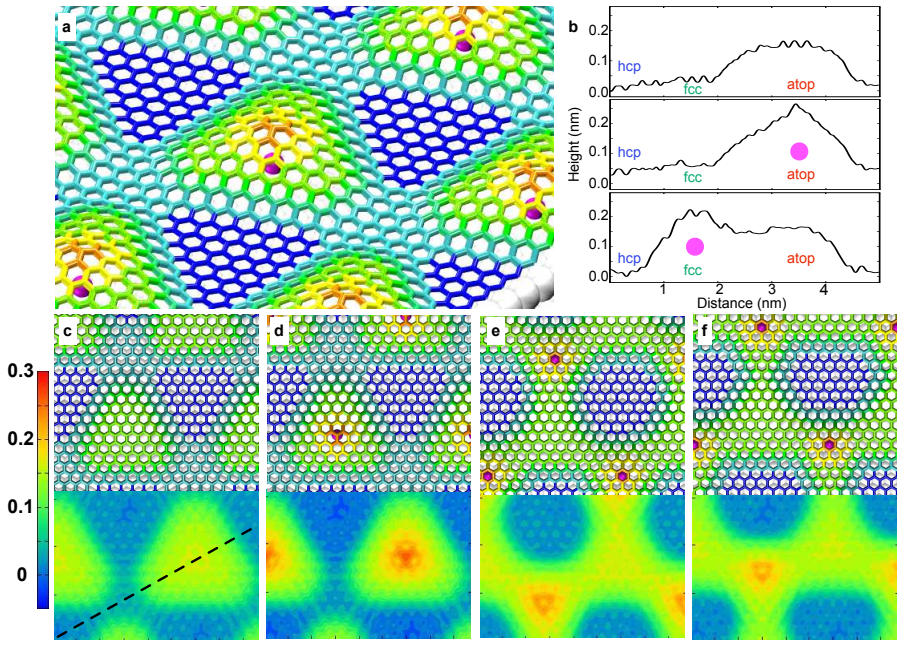

Figure 5: **Density functional theory results on the Ar implantation.** (a) Overview of the g/Ar/Ru(0001) structure with one Ar atom at the hill site. (b) Profile of the TH iso-current surface calculated along the diagonal of the moiré unit. The TH STM topography has been obtained with a bias potential of -1 eV and for a density of 10^3 e/nm^3. (c-f) Top view of the optimized structure and of TH STM topography obtained for the four studied systems: bare g/Ru (c), implanted g/Ar/Ru with Ar at the hill region (d), implanted g/Ar/Ru with Ar at the fcc region (e), and implanted g/Ar/Ru with Ar starting from the hcp region and moving to the fcc region (f).

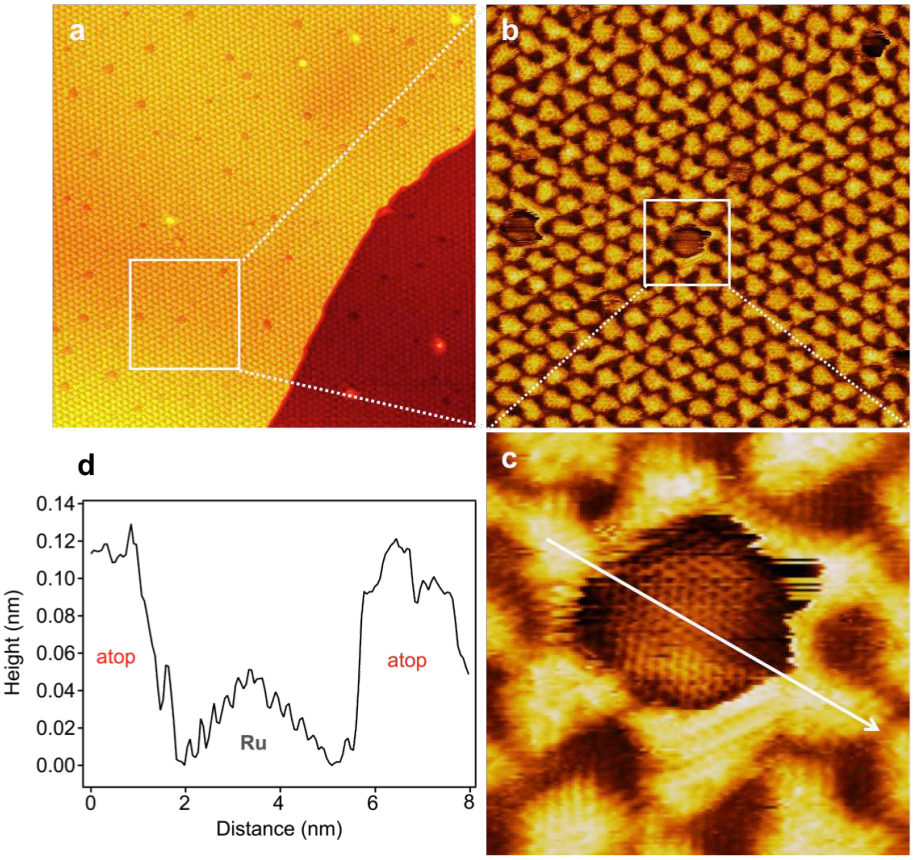

Figure 6: **"Can-opener" effect after annealing of g/Ar/Ru(0001) to 1000 K.** (sputter charge density 350 nC/cm^2) (a) Large-scale STM image (190×190 nm^2) showing 2 nm voids at atop sites. The bright flakes correspond to the cut-outs. U_t = -1.00 V, I_t = 0.50 nA. (b) Zoom-in (46×46 nm^2) of the white frame in (a) shows the regular graphene surface with four 2 nm voids. (c) High-resolution image (zoom-in image of the white frame in (b)) showing a void and the Ru atoms in this void, 8.8×8.8 nm^2, U_t = -1.00 V, I_t = 0.50 nA. (d) Cross-sectional profile along the white line in (c), illustrating the size of the void and the height difference between the void and the Ru substrate. The curve features of Ru atoms within the void is due to the tip effect.